Supplementary Materials

Gradient microcellular materials for broadband microwave absorption and multifunctional integration

Xiaojia Wang[1], Yichong Chen[1,2], Ke Lei[1], Xuwei Li[1], Jiayang Sun[1], Dongdong Hu[1], Ling Zhao[1,2]

[1]State Key Laboratory of Chemical Engineering and Low-Carbon Technology, Shanghai Key Laboratory of Multiphase Materials Chemical Engineering, School of Chemical Engineering, East China University of Science and Technology, Shanghai 200237, China.
[2]Shanghai Electronic Chemicals Innovation Institute, East China University of Science and Technology, Shanghai 201419, China.

Correspondence to: Dr. Yichong Chen, Prof. Ling Zhao, State Key Laboratory of Chemical Engineering and Low-Carbon Technology, Shanghai Key Laboratory of Multiphase Materials Chemical Engineering, School of Chemical Engineering, East China University of Science and Technology, Shanghai 200237, China. E-mail: chenyc@ecust.edu.cn; zhaoling@ecust.edu.cn

Structural and performance characterizations

(1) Microcellular Structure Characterization

The volume expansion ratio of microcellular samples (R_v) was measured by the drainage method and calculated from **Supplementary Equation (1)**:

$$R_v = \rho_0 / \rho_f \quad (1)$$

where ρ_0 is the density of FCIP/GP/SEBS composites (g cm^{-3}); ρ_f is the density of T FCIP/GP/SEBS microcellular materials (g cm^{-3}).

The microcellular morphology of the samples was examined using scanning electron microscopy (SEM; JSM660lv, JEOL Ltd., Japan). Prior to observation, Samples were quenched in liquid nitrogen for at least 5 minutes, then the cross-sections were subsequently coated with platinum. Energy-dispersive

spectroscopy (EDS) was employed to visualize the spatial distribution of fillers within the composite matrix via X-ray. The average cell diameter and cell density were determined by statistically analyzing at least 100 cells from the SEM images using Image-Pro Plus software.

The average cell diameter (d) is the average cell diameter in SEM image, which is calculated by **Supplementary Equation (2)**:

$$d=\frac{\Sigma d_i n_i}{\sum n_i} \tag{2}$$

Here, d_i is the cell diameter (μm) at a specific normalized location, n_i is the number of cells at that diameter.

The nucleation density (N) was calculated from **Supplementary Equation (3)**:

$$N=(n/A)^{3/2}\cdot R_v \tag{3}$$

where n is the number of cells in the SEM images; A is the area of the SEM image (cm^2).

Micro-computed tomography (Micro-CT; Skyscan 1272, Bruker Ltd., Belgium) was used to examine the cellular morphology. microcellular material were sectioned into 5 mm × 5 mm rectangular pieces and scanned at 80 kV and 142 μA. Two-dimensional (2D) cross-sections were reconstructed using NRecon software with Gaussian smoothing (level 2). Subsequent 2D and three-dimension (3D) morphological distributions was performed with CTAn software.

(2) Shear rheological characterization

The shear rheological characterization of FCIP/GP/SEBS composites was measured by a Rotational Rheometer (HAAKE, Germany). FCIP/GP/SEBS composites were hot-pressed into disks with a diameter of 35 mm and a thickness of 2 mm at 180 °C. The storage modulus G', the loss modulus G", the complex viscosity η* and the loss factor tan δ were measured at 180 °C in the frequency ranging from 100 to 0.1 rad s^{-1} under nitrogen atmosphere. A constant strain of 1% was applied for all tests to ensure measurements were conducted within the linear viscoelastic region.

(3) Tensile Property

FCIP/GP/SEBS composites were hot-pressed into dumbbell-shaped specimens at 180 °C. Tensile tests were conducted using a universal testing machine (3367, Instron, USA) at 25 ± 2 °C with a crosshead speed of 50 mm/min, following the ASTM-D638 standard. Tensile strength and elongation at break were recorded. Each sample was tested five times to ensure reliability and reproducibility of the results.

(4) Water Contact Angle

The wetting properties of the samples were characterized using a contact angle measuring instrument (JC2000D, POWEREACH, China). Prior to measurements, FCIP/GP/SEBS composites and their uniform microporous materials were quenched in liquid nitrogen for at least 5 minutes to expose cross-sections. Static water contact angles were measured via the sessile drop method by depositing 10 μL droplets of ultrapure water onto different regions of clean cross-sectional surfaces. After allowing the droplets to stabilize for 20 seconds, measurements were recorded. Five independent measurements were performed for each sample, and the static contact angles were subsequently determined by fitting the droplet images using ImageJ software.

(5) Electromagnetic Parameters

Electromagnetic parameters, including complex permittivity and complex permeability, were measured

using a vector network analyzer (Agilent E5071C, USA) in the frequency range of 2–18 GHz via the coaxial method. Prior to measurement, samples were cut into coaxial rings with an outer diameter of 7 mm and an inner diameter of 3.04 mm using a custom-designed mold.

The reflection loss, normalized input impedance (Z_{in}), and attenuation constant (α) were calculated from the measured electromagnetic parameters using the following **Supplementary Equations (4-6)**:

$$RL=20\log\left|\frac{Z_{in}-Z_0}{Z_{in}+Z_0}\right| \quad (4)$$

$$Z_{in}=Z_0\sqrt{\frac{\mu}{\varepsilon}}tanh\left(j\frac{2\pi fd\sqrt{\mu\varepsilon}}{c}\right) \quad (5)$$

$$Z=\frac{Z_{in}}{Z_0} \quad (6)$$

Here, Z_{in} and Z_0 are the normalized input impedances of the absorber and air, respectively. The d represents the thickness of the absorber. The ε' and ε'' represents real and imaginary parts of the complex permittivity (ε), respectively. The μ' and μ'' denote the real and imaginary parts of the complex permeability (μ), respectively.

(6) Magnetothermal Conversion

Under an alternating magnetic field (f = 350 kHz, H = 10.5 kA/m), the real-time surface temperature of the samples was monitored using an infrared thermal imaging camera (HM-TPH21Pro-3AQF, China). All measurements were performed at ambient temperature (25 °C) for a duration of 15 mins. Each sample was tested three times to ensure statistical significance.

(7) Photo-thermal-electric Conversion

The photothermal conversion performance of the samples was evaluated under simulated 1 sun irradiation using a solar simulator as the light source. Samples were placed on thermoelectric generator plates. Under ambient conditions (room temperature, ~25 °C), an infrared thermal imaging camera (HM-TPH21Pro-3AQF, China) and an electrometer (Keithley 6514/6517B, China) were simultaneously employed to monitor the surface temperature and the voltage output of the thermoelectric generator, respectively, over a period of 15 min. Each measurement was repeated three times to ensure statistical reliability.

(8) RCS Simulation

CST STUDIO SUITE 2022 was employed to simulate the far-field radar cross-section (RCS) of the samples under open boundary conditions.

About the vertical plate model, a perfect electric conductor (PEC) plate with dimensions of 200.0 × 200.0 mm² and a thickness of 1.0 mm was used in the simulations. The plate model was positioned in the Y–Z plane, and a linearly polarized plane wave was incident along the X-axis from the positive to the negative direction. The electric field polarization was oriented along the Z-axis. The far-field response was monitored at the peak frequency. The electromagnetic parameters of the models were obtained from the experimental data.

About the fighter aircraft model, the aircraft was positioned on the X-Y plane with its nose towards the positive X-axis. Here, the positive X-axis corresponds to $\Phi = 0°$, and the positive Z-axis corresponds to $\theta = 0°$. At the peak frequency, the RCS curves of the stealth aircraft, modeled with PEC, were simulated in both the uncoated configuration and the configuration coated with the gradient microcellular material.

Supplementary Figures and Tables

The viscoelastic properties of polymer materials play a crucial role in their foaming behavior[1]. Excessively high viscosity can hinder cell growth, whereas excessively low viscosity is detrimental to the structural stability of the cells. **Supplementary Figure 1** illustrates the variation curves of storage modulus (G'), loss modulus (G"), loss factor (tan δ= G"/G') and the complex viscosity (η) with frequency (ω) for samples with varying GP contents, respectively. With increasing GP content, G', G" and η of the samples increase markedly, whereas tan δ decreases. This behavior indicates that high particle filler content restricts the mobility of SEBS molecular chains, hindering its relaxation deformation. Meanwhile, the decrease in tan δ indicates that the samples gradually exhibit more pronounced solid-like characteristics. Under high-frequency conditions, molecular-chain relaxation is suppressed, leading to increases in both G' and G" with increasing ω. The decrease in η with increasing ω reflects typical shear thinning behavior[2]. The increase in the tan δ with increasing ω further indicates that internal friction and interfacial energy dissipation are enhanced at high frequencies, resulting in viscoelastic loss.

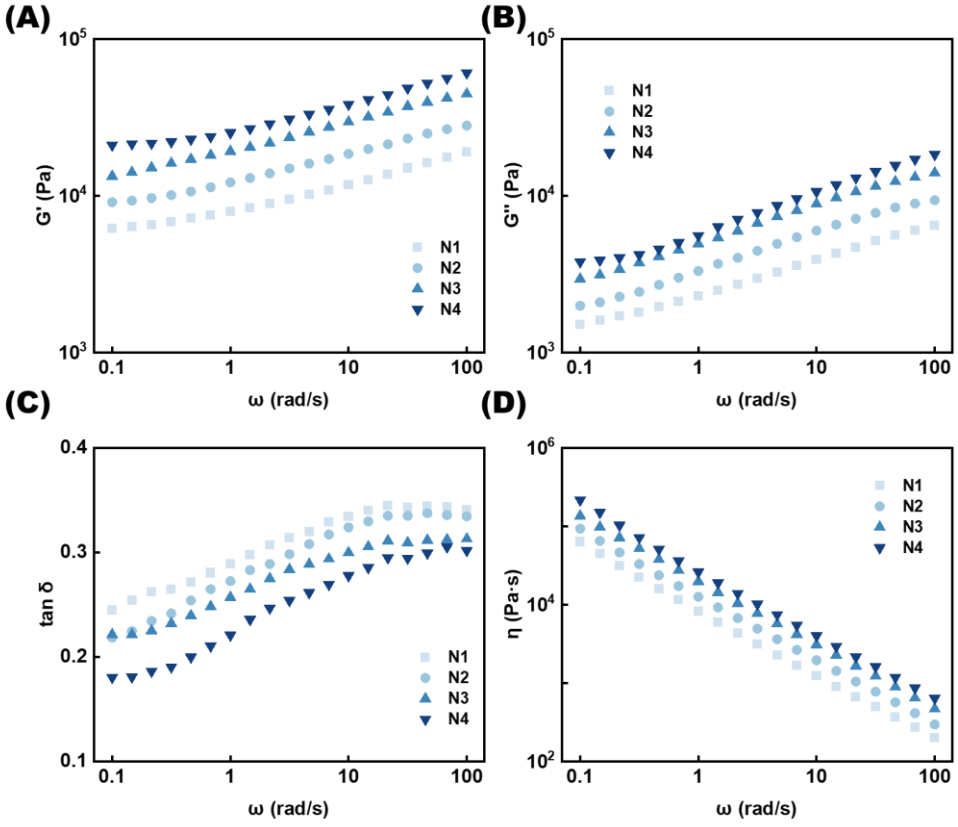

Supplementary Figure 1. Rheological Behavior. (A) Storage modulus (G'), (B) loss modulus (G"), (C) loss factor and (D) complex viscosity under 180°C conditions as a function of frequency.

Supplementary Figure 2 and **Supplementary Figure 3** present cross-sectional images of the microcellular materials obtained under different foaming conditions in **Supplementary Tables 1-3**. We systematically illustrating the effects of saturation temperature (T), saturation pressure (P), and saturation time (t) on the foaming behavior. GP promotes heterogeneous nucleation while simultaneously increasing the melt strength of the material[3], thereby restricting cell growth. As a result, increasing GP content

leads to higher cell density and smaller cell size. With increasing saturation temperature, the diffusion rate of N_2 increases and the melt viscoelasticity of the polymer decreases, which diminishes the resistance to cell growth, so the cell size becomes larger. Similarly, an increase in saturation pressure also results in larger cell size. Under incomplete saturation, N_2 diffuses along the thickness direction from the edge toward the center, thereby forming a concentration gradient of N_2[4,5]. As clearly shown in Fig. S3, with increasing saturation time, the cell density decreases and the cell size increases progressively from the edge to the center of the samples.

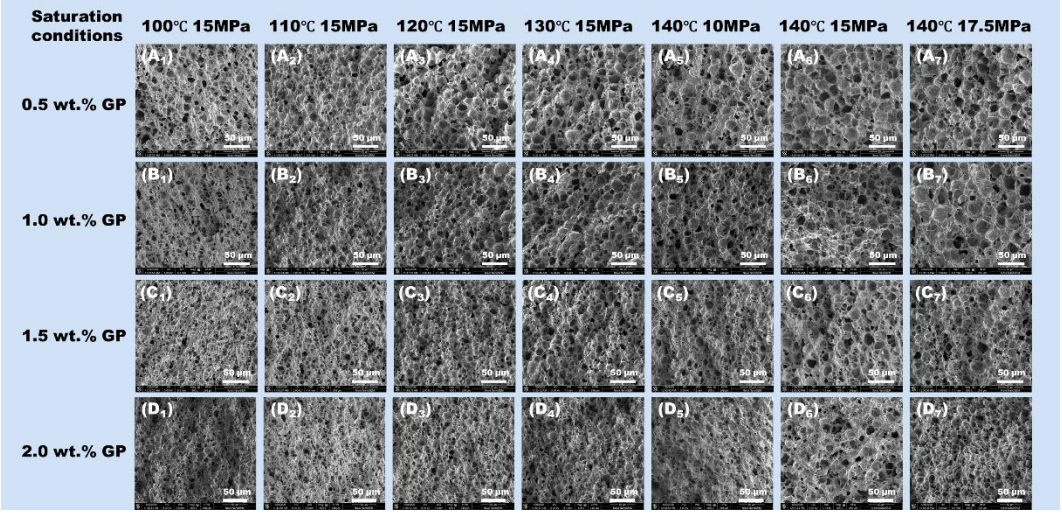

Supplementary Figure 2. Microstructural Characterization of Uniform Microcellular FCIP/CNTs/SEBS Materials with Saturation Time of 1 h at Different Foaming Conditions.

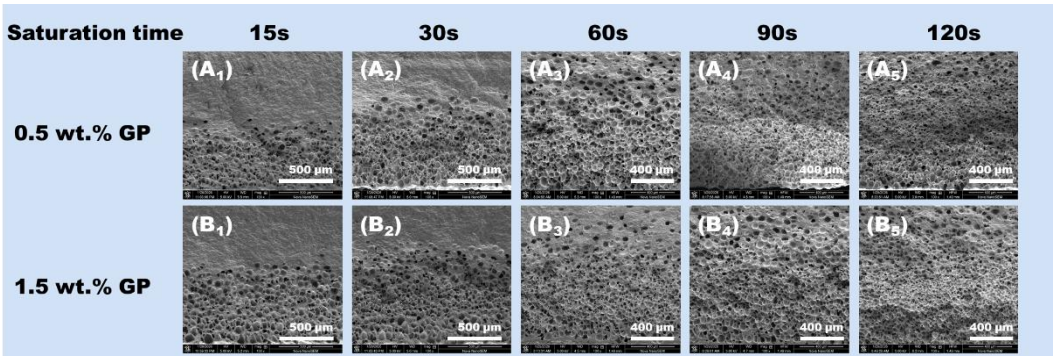

Supplementary Figure 3. Microstructural Characterization of Gradient Microcellular FCIP/CNTs/SEBS Materials at 180 ℃ and 15 MPa with Different Saturation time.

Supplementary Table 1. Process conditions and cell structure parameters of microcellular FCIP/GP/SEBS materials in Supplementary Figure 2.

Sample code	Raw material	T (℃)	P (MPa)	t	Sample code	Raw material	T (℃)	P (MPa)	t
a_1	N1	100	15	1.0 hour	b_1	100	15	1.0 hour	100
a_2	N1	110	15	1.0 hour	b_2	110	15	1.0 hour	110
a_3	N1	120	15	1.0 hour	b_3	120	15	1.0 hour	120
a_4	N1	130	15	1.0 hour	b_4	130	15	1.0 hour	130
a_5	N1	140	10	1.0 hour	b_5	140	10	1.0 hour	140
a_6	N1	140	15	1.0 hour	b_6	140	15	1.0 hour	140
a_7	N1	140	17.5	1.0 hour	b_7	140	17.5	1.0 hour	140
c_1	N3	100	15	1.0 hour	d_1	N4	100	15	1.0 hour
c_2	N3	110	15	1.0 hour	d_2	N4	110	15	1.0 hour
c_3	N3	120	15	1.0 hour	d_3	N4	120	15	1.0 hour
c_4	N3	130	15	1.0 hour	d_4	N4	130	15	1.0 hour
c_5	N3	140	10	1.0 hour	d_5	N4	140	10	1.0 hour
c_6	N3	140	15	1.0 hour	d_6	N4	140	15	1.0 hour
c_7	N3	140	17.5	1.0 hour	d_7	N4	140	17.5	1.0 hour

Supplementary Table 2. Process conditions and cell structure parameters of microcellular FCIP/GP/SEBS materials in Supplementary Figure 3.

Sample code	Raw material	T (℃)	P (MPa)	t	Sample code	Raw material	T (℃)	P (MPa)	t
a_1	N1	180	15	15 seconds	b_1	N3	180	15	15 seconds
a_2	N1	180	15	30 seconds	b_2	N3	180	15	30 seconds
a_3	N1	180	15	60 seconds	b_3	N3	180	15	60 seconds
a_4	N1	180	15	90 seconds	b_4	N3	180	15	90 seconds
a_5	N1	180	15	120 seconds	b_5	N3	180	15	120 seconds

Supplementary Table 3. Process conditions and cell structure parameters of microcellular FCIP/GP/SEBS materials for this work.

Sample code	T (℃)	P (MPa)	t	Cell type	Expansion ratio
U1	100	15	1.0 hour	Uniform	2.15
U2	105	15	1.0 hour	Uniform	2.16
U3	110	15	1.0 hour	Uniform	2.12
U4	120	15	1.0 hour	Uniform	2.03
G1	170	15	60 seconds	Gradient	2.16
G2	180	15	60 seconds	Gradient	1.97
G3	180	15	90 seconds	Gradient	2.08
G4	180	20	90 seconds	Gradient	1.98

The three-dimensional and two-dimensional plots of reflection loss (RL), shown in **Supplementary Figure 4-5**, illustrate the electromagnetic wave absorption performance of the samples.

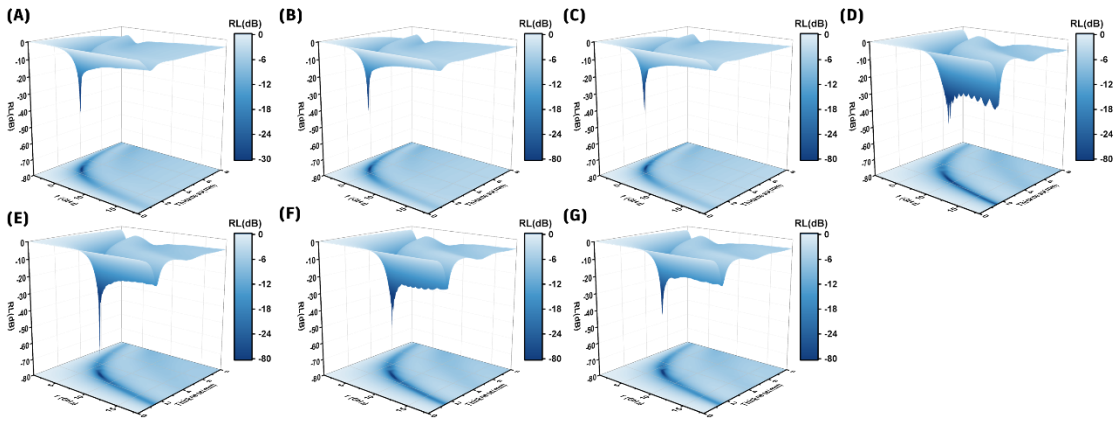

Supplementary Figure 4. Electromagnetic wave absorption properties for (A) N1, (B) N2, (C) N3, (D) U1, (E) U2, (F) U3, and (G) U4 depicted through three-dimensional reflection loss RL maps.

Supplementary Table 4. Comparison EMWA performances with several representative works in Figure 3O

Materials	-RL_{min} (dB)	EAB_{max} (GHz)	Reference
PP/CNT/Fe_3O_4 composite foams	47.82 (2.9 mm)	5.04 (3.0 mm)	[6]
TPU/CNT foam	51.8 (1.3mm)	3.3 (1.5mm)	[7]
PPy@BNC aerogel	53 (4 mm)	4.2 (3.7 mm)	[8]
SiC NWs/CMC foam	31 (3.3mm)	4.2 (3.3mm)	[9]
MWCNT/PVDF foams	31.0 (1.85mm)	7.8 (1.85mm)	[10]
CoNi@NC-CoNi@CNTs	59.92 (1.87mm)	5.6 (1.71 mm)	[11]
Re-Entrant Foams	51.85 (6.6 mm)	4.75 (6.2 mm)	[12]
Porous carbon@FeSiB	64.06 (1.42 mm)	4.7 (1.42 mm)	[13]
$Ti_3C_2T_x$ MXene composite	50.35 (1.30 mm)	6.01 (1.53 mm)	[14]
rGO/α-Fe_2O_3 composite hydrogel	33.5 (5.0mm)	6.4 (3.0mm)	[15]
HM-CoNC	69.52 (1.62 mm)	5.25 (1.69 mm)	[16]
Gradient microcellular FCIP/GP/SEBS (G1)	67.34 (2.21 mm)	9.40 (1.99 mm)	This work
Gradient microcellular FCIP/GP/SEBS (G2)	77.25 (2.44 mm)	9.16 (1.79 mm)	This work

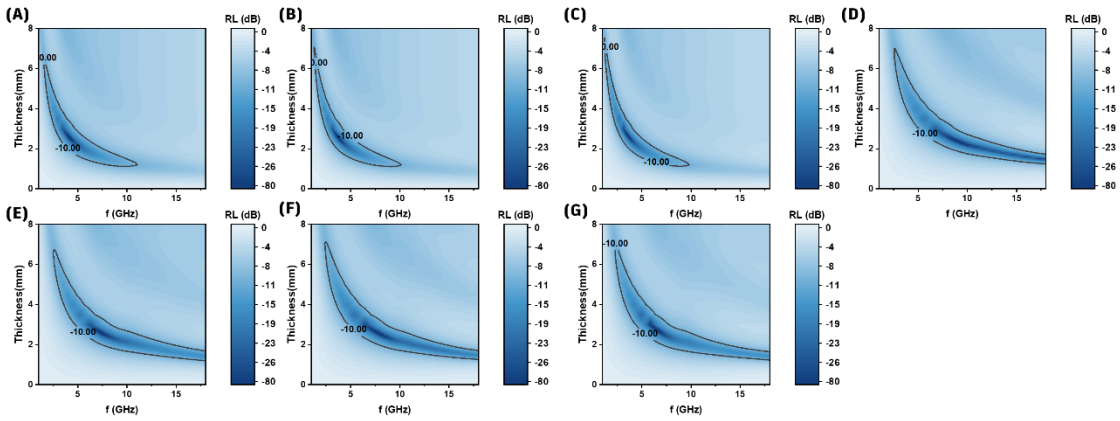

Supplementary Figure 5. Electromagnetic wave absorption properties for A) N1, (B) N2, (C) N3, (D) U1, (E) U2, (F) U3, and (G) U4 depicted through two-dimensional reflection loss RL maps.

Supplementary Figure 6A-C presents the simulated radar cross-section (RCS) maps of the PEC plate coated with G2 at 7.48 GHz, G3 at 7.38 GHz, and G4 at 7.33 GHz, confirming their excellent electromagnetic wave attenuation capability. **Supplementary Figure 6D-G** shows the simulated RCS distributions of the PEC and the G2-coated F-35 fighter model from the nose and dorsal aspects. These results demonstrate the considerable potential of G2 for radar stealth applications in military aircraft.

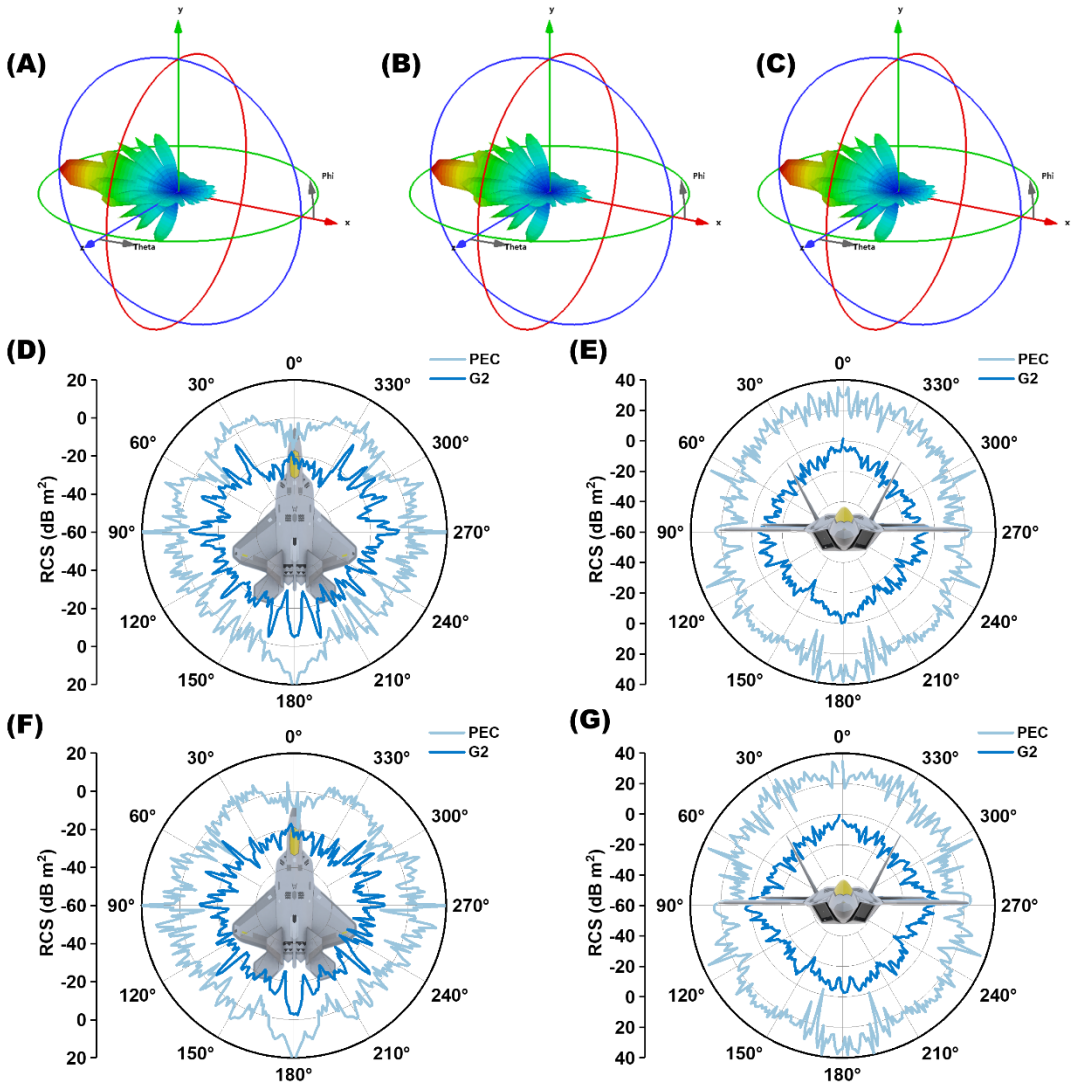

Supplementary Figure 6. RCS Simulation Results. Simulated RCS plots of the planar model for PEC covered with (A) G2 at 8.48 GHz, (B) G3 at 7.38 GHz and (C) G4 at 7.33 GHz; Forward view RCS of the fighter aircraft covered with G2 at 8.48 GHz for (D) horizontal and (E) vertical polarization, respectively and top view RCS of the aircraft covered with G2 at 7.48 GHz for (F) horizontal and (G) vertical polarization, respectively.

Supplementary Figure 7 illustrates electromagnetic parameters and attenuation of FCIP/GP/SEBS composites and their uniform microcellular materials.

Supplementary Figure 8 presents the Cole-Cole plots of the investigated samples, which were calculated according to **Supplementary Equation (7).**

$$(\varepsilon' - \frac{\varepsilon_S+\varepsilon_\infty}{2})^2 + (\varepsilon'')^2 = (\frac{\varepsilon_S+\varepsilon_\infty}{2})^2 \quad (7)$$

Here, ε' is the real parts of the complex permittivity, ε'' is the imaginary parts of the complex permittivity, ε_S is the static complex permittivity and ε_∞ is the complex permittivity at infinite frequency.

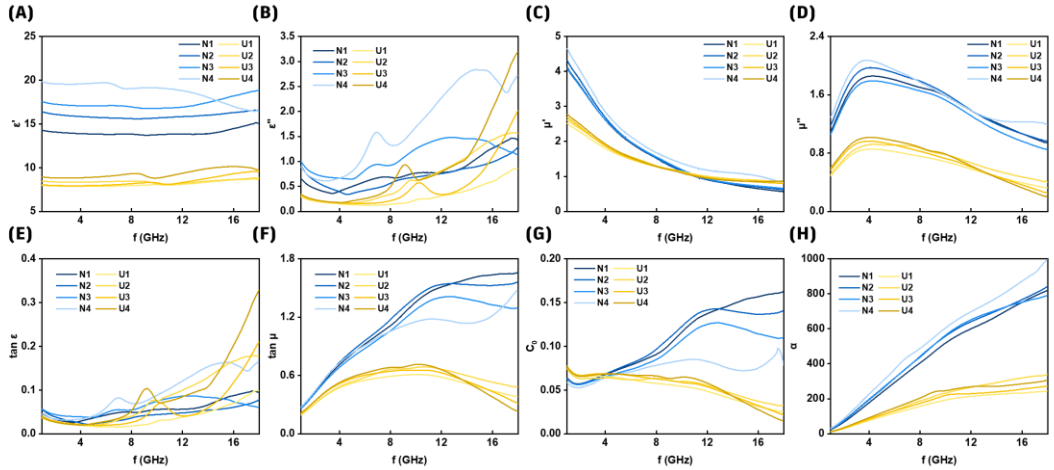

Supplementary Figure 7. Electromagnetic Parameters and Microwave Attenuation. (A) ε', (B)ε'', (C) μ' (D) μ'', (E) tanε, (F) tanμ, (G) C_0 and (H) α plots of FCIP/GP/SEBS composites and their uniform microcellular materials.

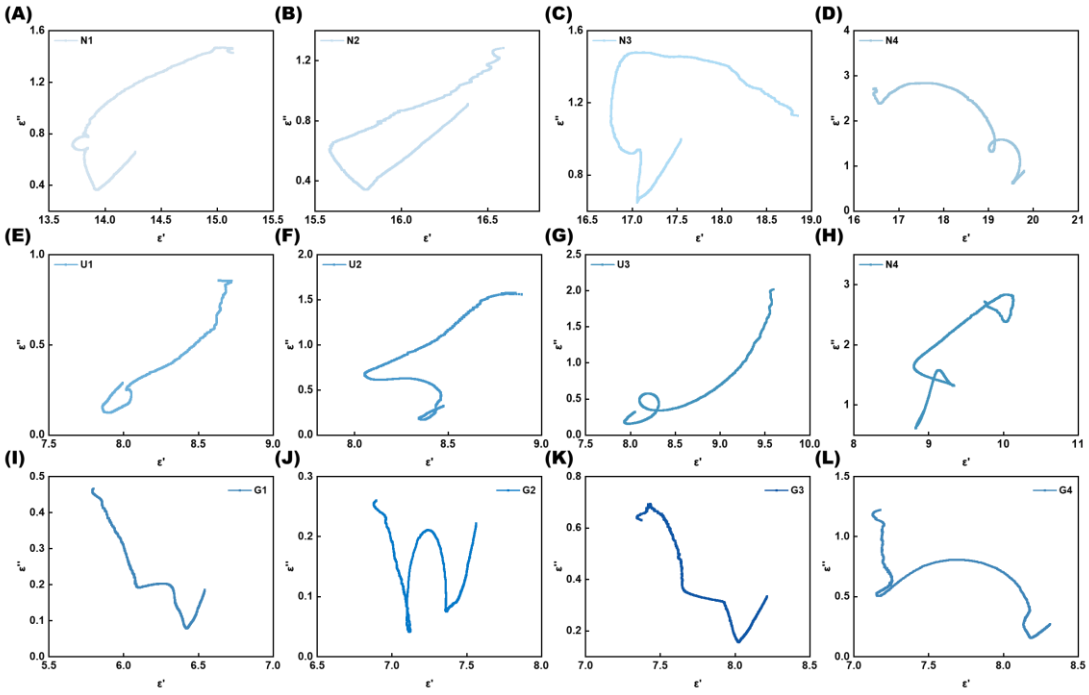

Supplementary Figure 8. Cole-Cole curve of (A) N1, (B) N2, (C) N3, (D) U4, (E) U1, (F) U2, (G) U3, (H) U4, (I) G1, (J) G2. (K) G3, and (L) G4.

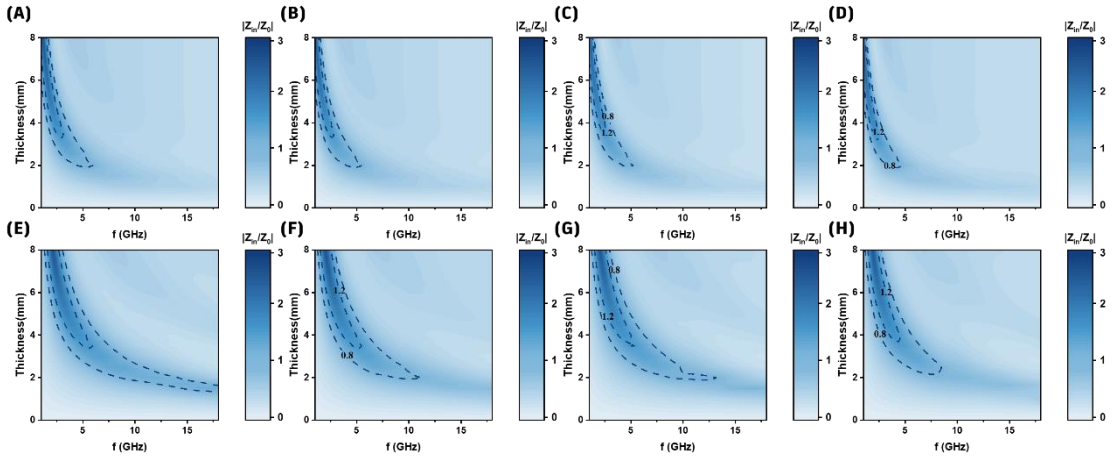

Supplementary Figure 9. Impedance matching of (A) N1, (B) N2, (C) N3, (D) N4, (E) U1 (F) U2, (G) U3, and (H) U4.

Supplementary Figure 9 shows the impedance matching maps of the samples demonstrating the crucial role of the gradient microcellular structure in optimizing impedance matching.

The water contact angles of the unfoamed samples N1, N2, N3, and N4 are shown in **Supplementary Figure 10,** indicating their hydrophilia.

Supplementary Figure 11 presents the infrared images of the magnetothermal conversion process of G1, G2, G3, G4, U4 and N4 at 0 min, 0.5 min, 1 min, 5 min and 10 min, demonstrating their excellent magnetothermal conversion performance.

Supplementary Figure 12 shows the infrared images obtained after 10 min of irradiation under one-sun illumination.

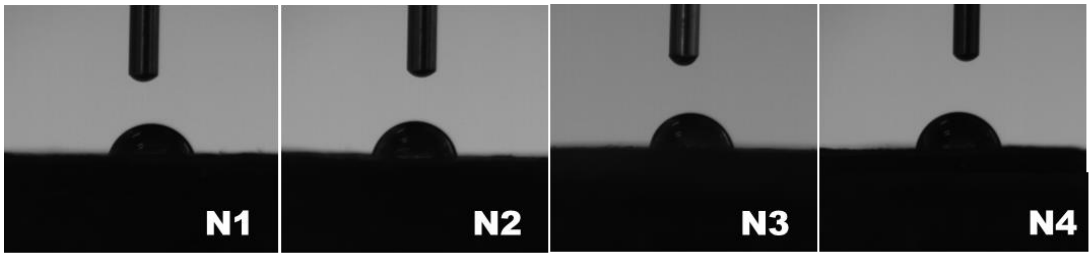

Supplementary Figure 10. Images of water contact angle.

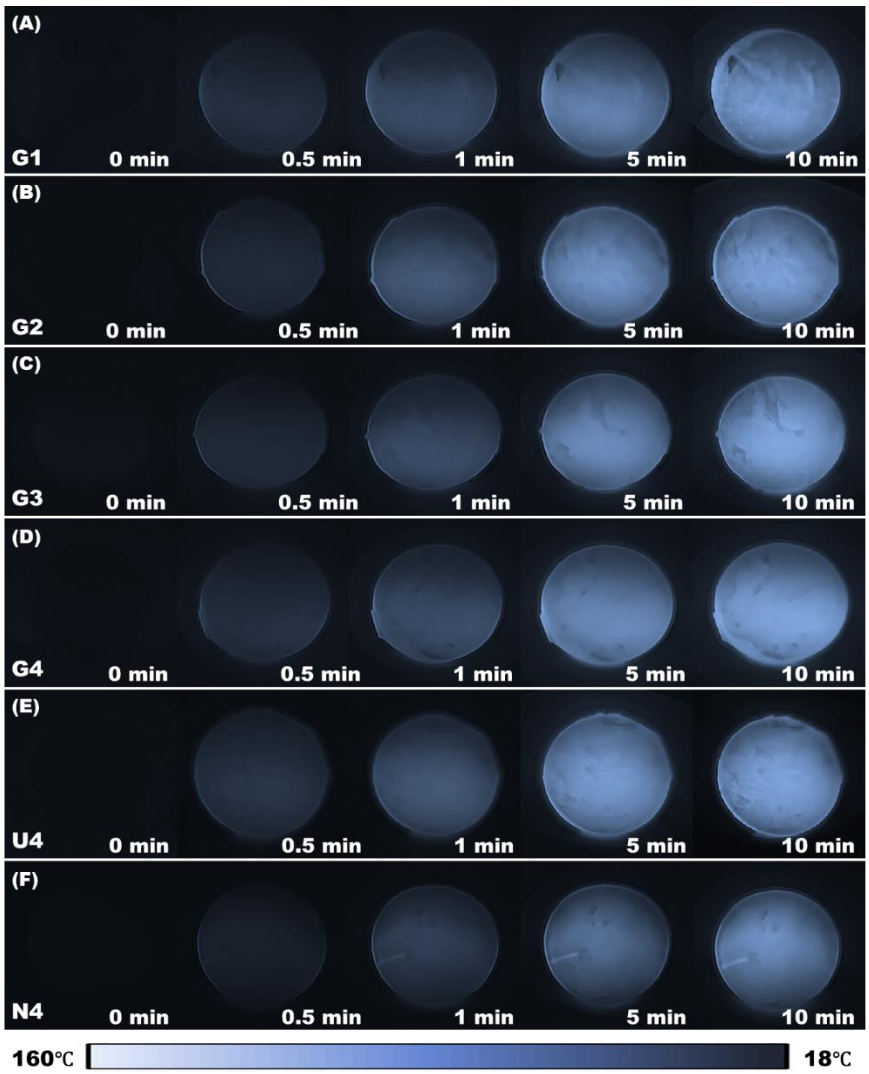

Supplementary Figure 11 Infrared images of magnetic heating process with (A) G1, (B) G2, (C) G3, (D) G4, (E) U4 and (F) N4.

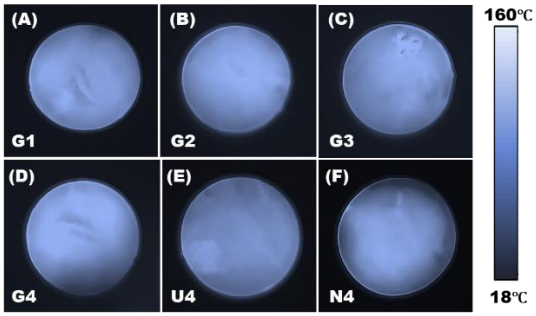

Supplementary Figure 12 Infrared images of light-induced heating process with (A) G1, (B) G2, (C) G3, (D) G4, (E) U4 and (F) N4.

Reference

[1] Zhao F, Zhang Z, Yang J, Yu J, Feng J, et al. Advanced nonlinear rheology magnetorheological finishing: A review[J]. Chinese Journal of Aeronautics, **2024**, 37(4): 54-92.

https://doi.org/https://doi.org/10.1016/j.cja.2023.06.006.

[2] Zhong W, Chen Y, Sun J, Wang X, Hu D, et al. Preparation of SEBS foam for new-generation sports protection and monitoring by microwave selective sintering[J]. Chemical Engineering Journal, **2025**, 515: 163494. https://doi.org/https://doi.org/10.1016/j.cej.2025.163494.

[3] Hou H-H, He X, Ma H, Zhou H-F, Wen B-Y, et al. Lightweight Ethylene-Vinyl Acetate Copolymer/Low-density Polyethylene/Carbon Nanotube Foams via Supercritical Carbon Dioxide Foaming for Piezoresistive Sensors[J]. Chinese Journal of Polymer Science, **2025**, 43(7): 1208-1221. https://doi.org/10.1007/s10118-025-3343-5.

[4] Zhu L, Wang G, Xu Z, Li X, Yang C, et al. A new microcellular foaming strategy to develop structure-gradient thermoplastic polyurethane foams with enhanced elasticity[J]. Materials & Design, **2023**, 234: 112325. https://doi.org/https://doi.org/10.1016/j.matdes.2023.112325.

[5] Wang G, Liu J, Zhao J, Li S, Zhao G, et al. Structure-gradient thermoplastic polyurethane foams with enhanced resilience derived by microcellular foaming[J]. The Journal of Supercritical Fluids, **2022**, 188: 105667. https://doi.org/https://doi.org/10.1016/j.supflu.2022.105667.

[6] Zhan H, Zhang Z, Yang A, Qian J, Antwi-Afari M F, et al. Multifunctional foams with oriented bimodal cellular structure and barbule-like surface fabricated by Bi-thermoplastic expanding microsphere mold-opening foaming[J]. Composites Part B: Engineering, **2026**, 310: 113173. https://doi.org/https://doi.org/10.1016/j.compositesb.2025.113173.

[7] Zhao B, Li X, Zeng S, Wang R, Wang L, et al. Highly Compressible Polymer Composite Foams with Thermal Heating-Boosted Electromagnetic Wave Absorption Abilities[J]. ACS Applied Materials & Interfaces, **2020**, 12(45): 50793-50802. https://doi.org/10.1021/acsami.0c13081.

[8] Lin X, Wang C, Zhang C, Guo Q, Hu C, et al. Asymmetric gradient-structured PPy@bacterial nanocellulose aerogels enable broadband microwave absorption via synergistic polarization-conduction loss[J]. Chemical Engineering Journal, **2025**, 520: 166529. https://doi.org/https://doi.org/10.1016/j.cej.2025.166529.

[9] Xiao S, Mei H, Han D, Dassios K G, Cheng L. Ultralight lamellar amorphous carbon foam nanostructured by SiC nanowires for tunable electromagnetic wave absorption[J]. Carbon, **2017**, 122: 718-725.

[10] Zhao B, Deng J, Zhao C, Wang C, Chen Y G, et al. Achieving wideband microwave absorption properties in PVDF nanocomposite foams with an ultra-low MWCNT content by introducing a microcellular structure[J]. Journal of Materials Chemistry C, **2020**, 8(1): 58-70. https://doi.org/10.1039/C9TC04575A.

[11] Liang Q, He M, Zhan B, Guo H, Qi X, et al. Yolk–Shell CoNi@N-Doped Carbon-CoNi@CNTs for Enhanced Microwave Absorption, Photothermal, Anti-Corrosion, and Antimicrobial Properties[J]. Nano-Micro Letters, **2025**, 17(1): 167. https://doi.org/10.1007/s40820-024-01626-8.

[12] Zhong W, Li X, Mi H-Y, Jing X, Dong B, et al. Architected absorbers with route guided trap mechanism for robust electromagnetic wave absorption[J]. Composites Part B: Engineering, **2026**, 312: 113309. https://doi.org/https://doi.org/10.1016/j.compositesb.2025.113309.

[13] Dong W, Tu S, Rehman S U, Chen C, Luo X, et al. Balancing electromagnetic wave loss capability and impedance matching of MOF derived porous carbon composite FeSiB based soft magnetic alloys to optimize the absorption performance[J]. Chemical Engineering Journal, **2025**, 517: 164370. https://doi.org/https://doi.org/10.1016/j.cej.2025.164370.

[14] Chen X, Wang X, Wen K, Zhang J, Zhao F, et al. Electrically aligned Ti3C2Tx MXene composite with multilayered gradient structure for broadband microwave absorption[J]. Carbon, **2023**, 203: 706-716. https://doi.org/https://doi.org/10.1016/j.carbon.2022.12.016.

[15] Zhang H, Xie A, Wang C, Wang H, Shen Y, et al. Novel rGO/α-Fe2O3 composite hydrogel: synthesis, characterization and high performance of electromagnetic wave absorption[J]. Journal of Materials Chemistry A, **2013**, 1(30): 8547-8552. https://doi.org/10.1039/C3TA11278K.

[16] Ling X, Zhang Y, Zhou Y, Wang Y, Xiong Y, et al. Hierarchical microstructure engineering of MOF-derived Co/N-doped carbon composites for tailored impedance matching and enhanced microwave absorption[J]. Journal of Alloys and Compounds, **2025**, 1041: 183464. https://doi.org/https://doi.org/10.1016/j.jallcom.2025.183464.